

Origin of the giant spin Hall effect in BiSb topological insulator

Takanori Shirokura¹, Kenichiro Yao¹, Yugo Ueda¹, and Pham Nam Hai^{1,2,3*}

¹*Department of Electrical and Electronic Engineering, Tokyo Institute of Technology,*

2-12-1 Ookayama, Meguro, Tokyo 152-0033, Japan

²*Center for Spintronics Research Network (CSRN), The University of Tokyo,*

7-3-1 Hongo, Bunkyo, Tokyo 113-8656, Japan

³*CREST, Japan Science and Technology Agency,*

4-1-8 Honcho, Kawaguchi, Saitama 332-0012, Japan

*Corresponding author: pham.n.ab@m.titech.ac.jp

The giant spin Hall effect (SHE) at room temperature is one of the most attractive feature of topological insulators (TIs) for applications to nano-scale spin devices. Its origin, however, remains a controversial problem. Here, we identify the origin of the giant SHE in BiSb thin films by measuring the spin Hall angle θ_{SH} under controllable contribution of surface and bulk conduction. We found that θ_{SH} of a $\text{Bi}_{0.6}\text{Sb}_{0.4}$ TI thin film takes colossal values (450 ~ 530 at 8 K, and 38 at 300 K), and is almost governed by contribution from the topological surface states. Meanwhile, θ_{SH} in a $\text{Bi}_{0.2}\text{Sb}_{0.8}$ semi-metallic thin film without topological surface states drastically decreases. Our results provide a quantitative tool for analysing the origin of the giant SHE in TI thin films, as well as a strategy for designing spin current source utilizing the surface states of TI in high-performance nano-scale spin devices.

The discovery of giant SHE with θ_{SH} exceeding unity at room temperature in several TI ultrathin films has attracted much attention for possible applications to nano spin devices, such as spin-orbit-torque magneto resistive random access memories and spin-torque oscillators.¹⁻⁴ An early experiment on the giant SHE in the well-studied Bi_2Se_3 TI assumed the surface state origin of the observed θ_{SH} (2 – 3.5), even though the Fermi level in Bi_2Se_3 lies in the conduction band and the contribution from the bulk conduction cannot be ignored.² The parallel conduction in the metallic surface and degenerated bulk states in Bi_2Se_3 cannot be quantitatively separated, and leads to large discrepancies in different measurements of θ_{SH} and even contradicting conclusion on the origin of the giant SHE in Bi_2Se_3 .^{5,6} More recently, systematic measurements of SHE in $(\text{Bi}_{1-x}\text{Sb}_x)_2\text{Te}_3$ TI thin films, whose Fermi level can be tuned to the band gap, show that SHE is almost twice larger when the Fermi level is in the valence band (bulk states dominant) than that when the Fermi level is in the band gap (topological surface states dominant), adding more controversy to the problem.⁷ From both fundamental and technological aspects, the origin of the giant SHE is the must solve problem for designing any nano spin devices using TI as the pure spin current source.

In this letter, we identify the origin of the giant SHE in BiSb thin films, by measuring the spin Hall angle θ_{SH} under controllable contribution of surface and bulk conduction. $\text{Bi}_{1-x}\text{Sb}_x$ ($0.07 < x < 0.22$) is the first three dimensional TI whose topological surface states have been detected using angle-resolved photoemission spectroscopy (ARPES)^{8,9}, scanning tunneling spectroscopy¹⁰, and quantum transport measurements.^{11,12} Recently, we observed that 10 nm-thick $\text{Bi}_{0.9}\text{Sb}_{0.1}$ thin films

with pseudo-cubic (012) surface show the highest room-temperature spin Hall conductivity ($1.3 \times 10^7 \frac{\hbar}{2e} \Omega^{-1} \text{m}^{-1}$) among all known materials thanks to the very large $\theta_{\text{SH}} \sim 52$ and high electrical conductivity $\sigma \sim 2.5 \times 10^5 \Omega^{-1} \text{m}^{-1}$, making $\text{Bi}_{1-x}\text{Sb}_x$ a very promising candidate for the pure spin current source in nano-scale spin devices.¹ In terms of fundamental properties, $\text{Bi}_{1-x}\text{Sb}_x$ has two unique features compared with other TIs. First, it has long Fermi wavelength (~ 40 nm) and much higher bulk mobility ($\sim 10^4 \text{ cm}^2 \text{V}^{-1} \text{s}^{-1}$) than other TIs, so that quantum confinement can occur in BiSb thin films even at room temperature. As a result, the band gap of BiSb thin films becomes larger at reduced thickness, and BiSb can become insulating in the region where it is semimetal in the bulk. For $\text{Bi}_{1-x}\text{Sb}_x$ thin films as thick as 90 nm, quantum confinement extends the insulating region from $x=0\%$ to at least 35%.¹³ Secondly, the Fermi level in BiSb is always in the band gap. Thus, BiSb thin films always have metallic surface states and insulating bulk states.^{13,14} This makes it possible to quantitatively evaluate the contribution of the surface states and bulk states to the giant SHE. Let us consider the electrical transport in a BiSb thin film for a general case shown in the inset of Fig. 1(a), where σ_{S} and σ_{B} are the conductivity of the surface and bulk states, t_{S} is the total penetration depth of the upper and lower surface states, t_{B} is the thickness of the bulk states, $\theta_{\text{SH}}^{\text{S}}$ and $\theta_{\text{SH}}^{\text{B}}$ are the spin Hall angle of the surface and bulk states, respectively. Because the Fermi level is in the band gap, the bulk conductivity follows $\sigma_{\text{B}} = \sigma_0 \exp(-\frac{E_{\text{g}}}{2k_{\text{B}}T})$, while σ_{S} is nearly temperature-independent. The temperature dependence of the total conductivity is given by $\sigma(T) = \frac{\sigma_{\text{S}} t_{\text{S}}}{t_{\text{B}}} + \sigma_0 \exp(-\frac{E_{\text{g}}}{2k_{\text{B}}T})$ (Eq. 1). Therefore, for $\text{Bi}_{1-x}\text{Sb}_x$ thin films with appropriate thickness

and band gap, we can quantitatively evaluate the contribution of the surface states to the total conductivity $\Gamma \equiv \frac{\sigma_S t_S}{\sigma_S t_S + \sigma_B t_B}$ by investigating the temperature dependence of the electrical resistivity, which is indispensable for identifying the origin of the giant SHE.

As a demonstration, we first show in Fig. 1(a) the temperature dependence of the normalised resistivity of $\text{Bi}_{0.89}\text{Sb}_{0.11}$ thin films with thickness of 10 nm (green dotted line), 41 nm (red dotted line), and 92 nm (blue dotted line), respectively. The solid lines are fitting curves using Eq. (1), which show good agreement with the experimental data, yielding $\Gamma(300 \text{ K}) = 20.2 \%$, $E_g = 34.2 \text{ meV}$ for the 92 nm-thick film, $\Gamma(300 \text{ K}) = 38.3 \%$, $E_g = 66.6 \text{ meV}$ for the 41 nm-thick film, and $\Gamma(8 - 300 \text{ K}) = 100 \%$ for the 10 nm-thick film. One can see that the bulk conduction is dominant for the 92 nm-thick film. As the thickness is reduced to 41 nm, the surface state contribution began to rise significantly due to the increasing band gap. When the thickness is further reduced to 10 nm, the band gap becomes large enough so that metallic surface conduction is dominant. Thus, BiSb with intermediate thickness (40 – 50 nm) has tunable surface and bulk conduction, and is suitable for studying the origin of the giant SHE. In this work, we prepare two samples; one is MnAs (5 nm) / $\text{Bi}_{0.6}\text{Sb}_{0.4}(001)$ (50 nm) (sample A) and the other is MnAs (3.2 nm) / $\text{Bi}_{0.2}\text{Sb}_{0.8}(001)$ (50 nm) (sample B), grown on GaAs(111)A substrates by molecular beam epitaxy (MBE), whose schematic cross section are shown in Fig. 1(b). Here, the hexagonal coordinate indexing and the cubic coordinate indexing are used for BiSb and GaAs, respectively. The temperature dependence of the resistivity reveals that the $\text{Bi}_{0.6}\text{Sb}_{0.4}$ (50 nm) layer behaves as a topological insulator with a band gap of 33.2

meV and mixing of surface and bulk conduction, and that Γ changes from 60 % to 100 % when temperature decreases from 300 K to 8 K. On the other hand, the $\text{Bi}_{0.2}\text{Sb}_{0.8}$ (50 nm) layer behaves purely as a semimetal layer (see Supplementary Note 1) .¹³ The MnAs top layers have in-plane magnetisation for detection of the injected spin current. These samples are patterned into Hall bars with dimension of $50 \mu\text{m} \times 100\text{-}200 \mu\text{m}$ by Ar ion milling and photolithography for transport measurements. To study the spin Hall effect of BiSb, we use the direct current (DC) planar Hall technique with an in-plane rotating magnetic field^{3,15,16} over a wide range of temperature from 8 K to 300 K. Figure 1(c) shows the schematic experimental setup and the coordinate system of the DC planar Hall method. A DC current I is injected to the bi-layer along the x -direction. The Hall resistance R_H is measured under a constant magnetic field $H_{\text{ext}} = 5 \text{ kOe}$ rotating in the xy -plane for $\theta = 0 - 360^\circ$ with respect to the x axis. The SHE from the BiSb layer generates a transverse field-like effective field H_T and a perpendicular anti-damping-like effective field H_{SO} acting on the MnAs layer. Here, H_{SO} is given by $H_{\text{SO}} = \frac{\hbar\theta_{\text{SH}}J_C}{2eM_S t_{\text{FM}}}(-\hat{\sigma} \times \hat{m}) = -\frac{\hbar\theta_{\text{SH}}J_C}{2eM_S t_{\text{FM}}}(\cos\phi)\hat{z}$, where \hbar is the Dirac's constant, J_C is the charge current density in the BiSb layer, e is the electronic charge, M_S is the saturation magnetisation of the MnAs layer, t_{FM} is the thickness of the MnAs, $\hat{\sigma}$ is the spin polarization unit vector, and \hat{m} is the magnetisation unit vector. ϕ is the magnetisation direction in the xy -plane with respect to the x -axis, and given by $\phi(\pm I) = \text{Tan}^{-1}\{(\sin\theta \pm \delta)/\cos\theta\}$, where $\delta = H_T/H_{\text{ext}}$. Since H_{SO} generates a z -component of the magnetisation, the Hall resistance R_H is given by

$$R_H(\pm I) = R_{\text{PHE}} \sin 2\phi + R_{\text{AHE}}^{\text{SO}} \cos \phi + R_{\text{AHE}}^x \cos \phi + R_{\text{AHE}}^y \sin \phi + C \quad (2)$$

The first term comes from the planar Hall effect (PHE). The second term comes from the anomalous Hall effect (AHE) due to the H_{SO} -induced z-component of the magnetisation, and the third and fourth term arise from small mis-alignment of the H_{ext} rotating surface from the xy -plane. The fifth term is the experimental Ohmic offset.

Figure 2 shows the θ -dependence of R_{H} as a function of I in sample A at 8 K and those in sample B at 10 K. The blue circles show the measurement data and the red solid lines show the fitting results using Eq. (2) with R_{PHE} , $R_{\text{AHE}}^{\text{SO}} + R_{\text{AHE}}^x$, R_{AHE}^y , C and δ as fitting parameters. The fitting curves agree very well with the experimental data. R_{H} of sample A shows strong dependence on the input current, as shown in Fig. 2(a) – 2(f). In contrast, much weaker input current dependence is observed for sample B, as shown in Fig. 2(g) – 2(l). Hence, H_{SO} in sample A is much stronger than that in sample B. Because $R_{\text{AHE}}^{\text{SO}}$ depends on J_{C} while R_{AHE}^x does not, we can extract $R_{\text{AHE}}^{\text{SO}}$ as a function of J_{C} . Figure 3 shows the J_{C} -dependence of $R_{\text{AHE}}^{\text{SO}}$ of sample A (Fig. 3(a) – 3(h)) and sample B (Fig. 3(i) – 3(l)) as a function of temperature, respectively. Here, for calculation of J_{C} , we calibrated the conductivity of the MnAs layer from the amplitude of PHE (R_{PHE}) (see Supplementary Note 2). The blue dots and the blue solid lines show the measurement data and linear fitting of $R_{\text{AHE}}^{\text{SO}}$, respectively. The red solid lines show H_{SO} calculated from $R_{\text{AHE}}^{\text{SO}} \frac{dH_{\text{perp}}}{dR_{\text{AHE}}} \frac{H_{\text{ext}} + H_{\text{deg}}}{H_{\text{deg}}}$, where $\frac{dR_{\text{AHE}}}{dH_{\text{perp}}}$ is the gradient of the anomalous Hall resistance vs. perpendicular magnetic field (see Supplementary Note 3), and $\frac{H_{\text{ext}} + H_{\text{deg}}}{H_{\text{deg}}}$ is the correction factor for the large in-plane $H_{\text{ext}} = 5$ kOe and the small demagnetising field $H_{\text{deg}} = 4\pi M_{\text{s}} = 5$ kOe of the MnAs layers. Here, we took into

account the shunt circuit effect of the bias current, the short circuit effect of the Hall voltage, and the normal Hall effect in estimating $\frac{dR_{\text{AHE}}}{dH_{\text{perp}}}$ (Supplementary Note 3).¹⁷ In Fig. 3(a) – 3(h), the sign of H_{SO} in sample A is the same as that of Pt,^{15,18} and agrees with previous reports on Bi-based TIs.^{1-3,7} However, the sign of H_{SO} in sample B is reversed, demonstrating the fundamental difference in the origin of H_{SO} between sample A (TI) and sample B (semimetal).

Figure 4 (a) shows the temperature dependence of θ_{SH} in sample A (blue dots) and sample B (red dots) calculated by $\theta_{\text{SH}} = \frac{2eM_{\text{S}t_{\text{FM}}}H_{\text{SO}}}{\hbar J_{\text{C}}}$. For a reference, we also show the room-temperature θ_{SH} (=52) of a 10 nm-thick BiSb(012) layer (green dot in Fig. 4(a)).¹ Note that θ_{SH} calculated in this way is the nominal value of the whole BiSb layers with contribution from both the surface and the bulk states. θ_{SH} of sample A dramatically increases from 38 at 300 K to a colossal value of 450 at 8 K, and is significantly larger than that of sample B (-4.4 at 10 K and -0.98 at 154 K). The much higher θ_{SH} in sample A is an evidence for the important contribution of surface states to the giant SHE in BiSb TI thin films.

The colossal value of $\theta_{\text{SH}} = 450$ at 8 K corresponds to the very large spin Hall conductivity of $\sigma_{\text{SH}} \sim 1.1 \times 10^8 \frac{\hbar}{2e} \Omega^{-1} \text{m}^{-1}$ for BiSb, which is even higher than the “charge” conductivity of silver, the most conductive metal ($\sigma \sim 6.3 \times 10^7 \Omega^{-1} \text{m}^{-1}$). To check that we do not overestimate θ_{SH} at low temperatures due to thermoelectric effects, such as the anomalous Nernst effect in the MnAs layer, we independently estimate θ_{SH} from the amplitude of the planar Hall resistance R_{PHE} as a function of the bias current (see Supplementary Note 2). Our analysis shows that R_{PHE} should be reduced by

$$\frac{\Delta R_{\text{PHE}}}{R_{\text{PHE}}} = -\frac{(H_{\text{SO}})^2}{2(H_{\text{ext}} + H_{\text{deg}})^2} = -\frac{(\alpha I)^2}{2(H_{\text{ext}} + H_{\text{deg}})^2} \text{ (see Eq. S6 in the Supplementary Note 2). Here, } \alpha \text{ is}$$

the proportional constant between H_{SO} and I , and directly related to θ_{SH} . In contrast, any thermoelectric effects would cause a linear dependence of R_{PHE} on I . Our data show a clear quadratic and no linear dependence of R_{PHE} on I for the sample A (Fig. S2 in Supplementary Note 2, also see Supplementary Note 4). Thus, thermoelectric effects are absent or negligible in our bi-layers. Furthermore, by fitting to the $\frac{\Delta R_{PHE}}{R_{PHE}} - I$ data, we can independently estimate α and θ_{SH} . Our data at 8 K yields $\alpha = 0.22$ kOe/mA and $\theta_{SH} = 530$, which is even higher than $\theta_{SH} = 450$ estimated from the R_{AHE}^{SO} . The 15% difference between the two methods may be due to uncertainty in estimation of the $\frac{dR_{AHE}}{dH_{\text{perp}}}$ gradient used in the former method. Our results double check the colossal θ_{SH} of BiSb at low temperature.

Next, we quantitatively evaluate the contribution of the surface states to the nominal θ_{SH} . Assuming the parallel conduction model in the inset of Fig. 1(a) with $t_B \gg t_S$, θ_{SH} for a TI layer is given by (Supplementary Note 5),

$$\theta_{SH} = \Gamma \frac{t_B}{t_S} \theta_{SH}^S + \frac{2e}{\hbar} \frac{\sigma_{SH}^B t_B}{\sigma_S t_S + \sigma_B t_B}, \quad (3)$$

where $\sigma_{SH}^B = \frac{\hbar}{2e} \theta_{SH}^B \sigma_B$ is the spin Hall conductivity of bulk states. Eq. (3) explains why there are large discrepancies in different measurements of θ_{SH} for the case of Bi_2Se_3 with different thickness and bulk conductivity. Even if we assume σ_S and t_S are intrinsic parameters of a TI and do not change with the growth condition, θ_{SH} can still vary with σ_B , t_B , and Γ . In the limit of $\sigma_S t_S \ll \sigma_B t_B$ (bulk conduction is dominant), θ_{SH} is equal to θ_{SH}^B , which is typically of order of 0.1. In the opposite case of $\sigma_S t_S \gg \sigma_B t_B$, θ_{SH} approaches $\frac{t_B}{t_S} \theta_{SH}^S$ but still depends on the ratio $\frac{t_B}{t_S}$. In general, in order to understand the origin of SHE in TI, it is necessary to know the values of the parameters in Eq. (3). In

our case of BiSb, $\sigma_S t_S$ and $\sigma_B t_B$ can be experimentally deduced from the temperature dependence of the total conductivity and fitting to Eq. (1). However, the exact value of t_S is unknown. Thus, to

evaluate the surface and the bulk contribution, we introduce the nominal “sheet spin Hall angle”

$$q_{\text{SH}} \equiv \frac{\theta_{\text{SH}}}{t_B + t_S} \approx \frac{\theta_{\text{SH}}}{t_B} \text{ for the whole layer, and the “surface sheet spin Hall angle” } q_{\text{SH}}^{\text{S}} \equiv \frac{\theta_{\text{SH}}^{\text{S}}}{t_S} \text{ for the}$$

surface states. Substituting q_{SH} and q_{SH}^{S} to Eq. (3), we obtain $q_{\text{SH}}^{\text{S}} = \frac{1}{\Gamma} q_{\text{SH}} - \frac{2e}{\hbar} \frac{\sigma_{\text{SH}}^{\text{B}}}{\sigma_S t_S}$ (4), which

reflects the intrinsic SHE of the surface states. Using this equation, we can estimate q_{SH}^{S} using the

experimental values of Γ , q_{SH} , $\sigma_S t_S$, and the calculated value of $\sigma_{\text{SH}}^{\text{B}} \sim -9.3 \times 10^4 \frac{\hbar}{2e} \Omega^{-1} \text{m}^{-1}$ from

the first principle calculation.¹⁹ Figure 4 (b) shows the values of q_{SH}^{S} (blue dots) and q_{SH} (blue

squares) of sample A as a function of temperature. q_{SH}^{S} rapidly increases from 1.3 nm^{-1} at room

temperature to about 9 nm^{-1} at temperatures below 100 K. The inset in Fig. 4 (b) shows the

contribution of the bulk states to the nominal sheet spin Hall angle, $R \equiv \frac{2e}{\hbar} \frac{|\sigma_{\text{SH}}^{\text{B}}|}{q_{\text{SH}} (\sigma_S t_S + \sigma_B t_B)}$, which

is always lower than 1%. Our results clearly show that the giant SHE in BiSb TI thin film originates

from the surface states, even in the $\text{Bi}_{0.6}\text{Sb}_{0.4}$ layer as thick as 50 nm. Note that although the

room-temperature $q_{\text{SH}}^{\text{S}} = 1.3 \text{ nm}^{-1}$ of the 50 nm-thick $\text{Bi}_{0.4}\text{Sb}_{0.6}(001)$ layer is already large, it is still

smaller than the room-temperature value ($q_{\text{SH}}^{\text{S}} = 5.2 \text{ nm}^{-1}$) of a 10 nm-thick $\text{BiSb}(012)$ layer (green

dot in Fig. 4(b)).¹ The difference may come from the fact that there are three Dirac cones on the

pseudo-cubic surface of $\text{BiSb}(012)$, which were theoretically predicted²⁰ and experimentally

confirmed by ARPES observation,²¹ comparing with one Dirac cone on the hexagonal surface of

BiSb(001). Since Dirac cones on the surface of TI are monopoles of Berry flux with the same chirality, more Dirac cones mean larger total Berry flux and thus higher surface spin Hall conductivity. The correlation between the sheet spin Hall angle and the numbers of Dirac cones on the BiSb surfaces gives another evidence for the surface state origin of the giant SHE in BiSb.

In summary, by quantitatively evaluating the SHE under controllable contribution of surface and bulk conduction at various temperature and surface orientation, we have shown that the giant SHE in BiSb is entirely governed by the surface states from 8 K up to room temperature. Our results provide a quantitative tool for analysing the origin of the giant SHE in TI thin films, as well as a strategy for designing spin current source utilizing the surface states of TI in high-performance nano-scale spin devices.

Acknowledgement

This work is supported by Grant-in-Aid for Challenging Exploratory Research (No. 16K14228), Nanotechnology platform 12025014 (F-17-IT-0011) from MEXT, and JST CREST (JPMJCR18T5). Data of sample B are obtained with supports from TDK Corporation. We thank the Material Analysis Division and Laboratory for Future Interdisciplinary Research of Science and Technology at Tokyo Institute of Technology, and M. Tanaka Laboratory at University of Tokyo for their technical supports.

Methods

MBE growth. The thin films were grown on semi-insulating GaAs(111)A substrates by using ultrahigh vacuum MBE system. After the surface oxide layer of the GaAs substrate was removed by annealing at 580°C, a GaAs buffer layer was grown to obtain an atomically smooth surface. Then, a 50 nm-thick Bi_{0.6}Sb_{0.4}(001) or Bi_{0.2}Sb_{0.8}(001) layer was grown at a substrate thermocouple temperature of 200°C. Finally, a 5 nm (or 3.2 nm)-thick MnAs(001) layer was grown on top of the BiSb layer at a substrate thermocouple temperature of 320°C as the ferromagnetic layer. A 23.3 nm-thick MnAs(001) single layer was also grown on a GaAs(111)B substrate as a reference.

Hall bar fabrication. The samples were patterned into Hall bar structures by standard optical lithography and Ar ion milling.

SOT measurements. A Keithley 2400 Sourcemeter was used as the current source for DC planar Hall measurements. The Hall voltage was measured using a Keithley 2002 Multimeter. The Hall bars were mounted inside a Gifford-McMahon cryostat equipped with a computer-controlled rotatable electromagnet.

Author Contributions

T.S. and K.Y. (equal contribution) grew the MnAs/BiSb bi-layers, fabricated the Hall devices, and performed Hall effect measurements; Y. U. evaluated the conductivity of various BiSb layers; P.N.H. planned the experiments; T.S., K.Y, P.N.H. analysed the data. T.S. and P.N.H wrote the manuscript, with comments from K.Y. and Y. U.

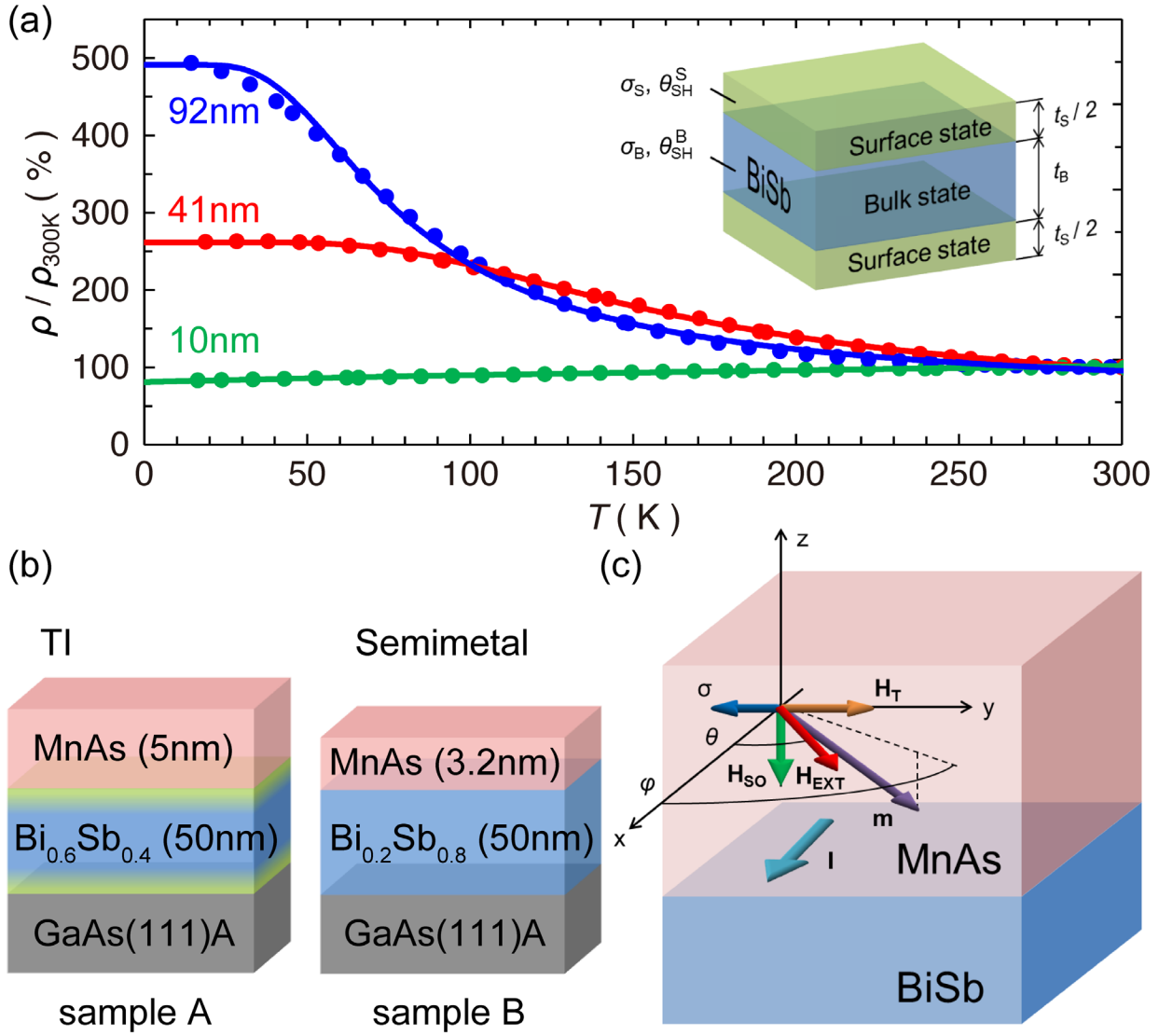


FIG. 1. (a) Temperature dependence of the normalised resistivity in Bi_{0.89}Sb_{0.11} thin films with thickness of 10 nm (green), 41 nm (red) and 92 nm (blue). Dots and solid lines show the experimental data and fitting to a parallel conduction model of BiSb (inset). (b) Schematic structure of a MnAs / BiSb (TI) bi-layer (sample A) and a MnAs / BiSb (semimetal) bi-layer (sample B). (c) Schematic illustration of the experiment setup and coordination system for DC planar Hall measurements.

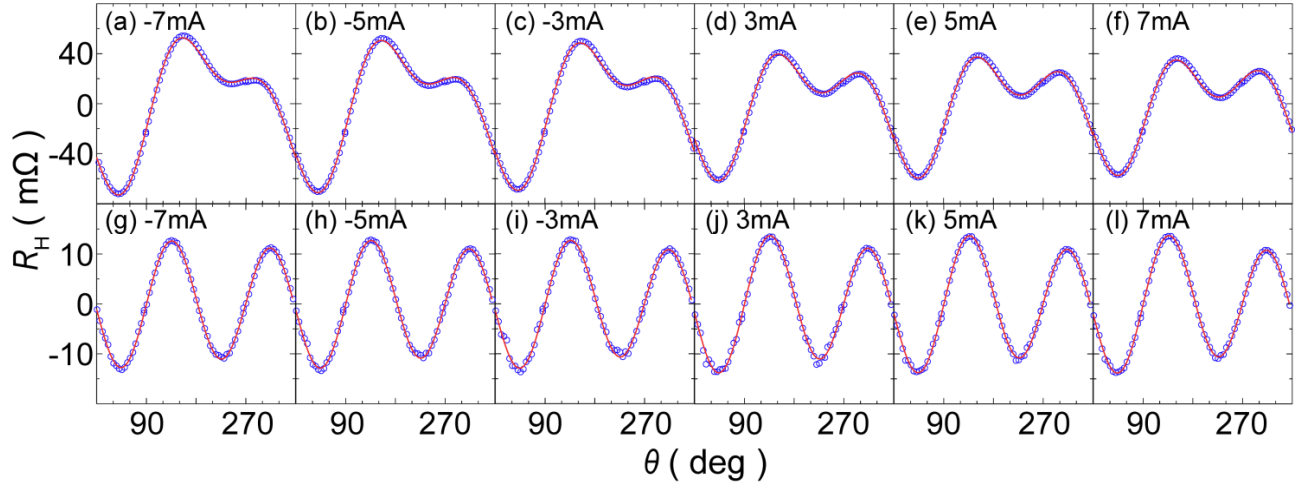


FIG. 2. In-plane magnetic field direction (θ)-dependence of the Hall resistance R_H . **(a) – (f)** sample A at 8 K, and **(g) – (l)** sample B at 10 K. The bias current is changed from -7 mA to 7 mA. Blue circles are experiment data and red lines are fitting using Eq. (2) in text.

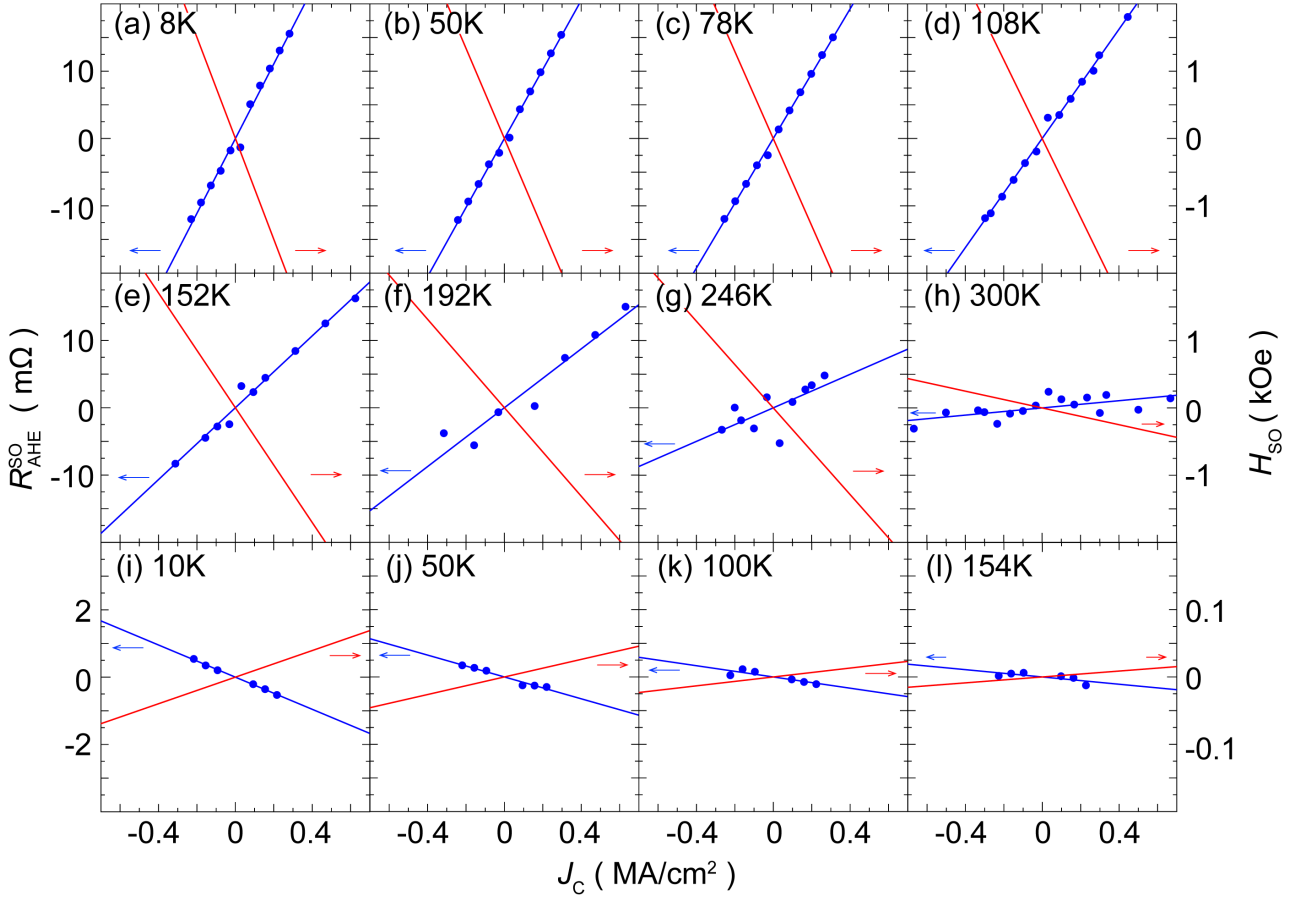


FIG. 3. Amplitude of the anomalous Hall resistance $R_{\text{AHE}}^{\text{SO}}$ arising from the spin-orbit effective field H_{SO} , as a function of the charge current density in the BiSb layer at various temperatures for **(a)-(h)** sample A and **(i)-(l)** sample B. Blue dots and blue lines are the experimental data and linear fitting of $R_{\text{AHE}}^{\text{SO}}$, while red solid lines show the calculated H_{SO} , respectively.

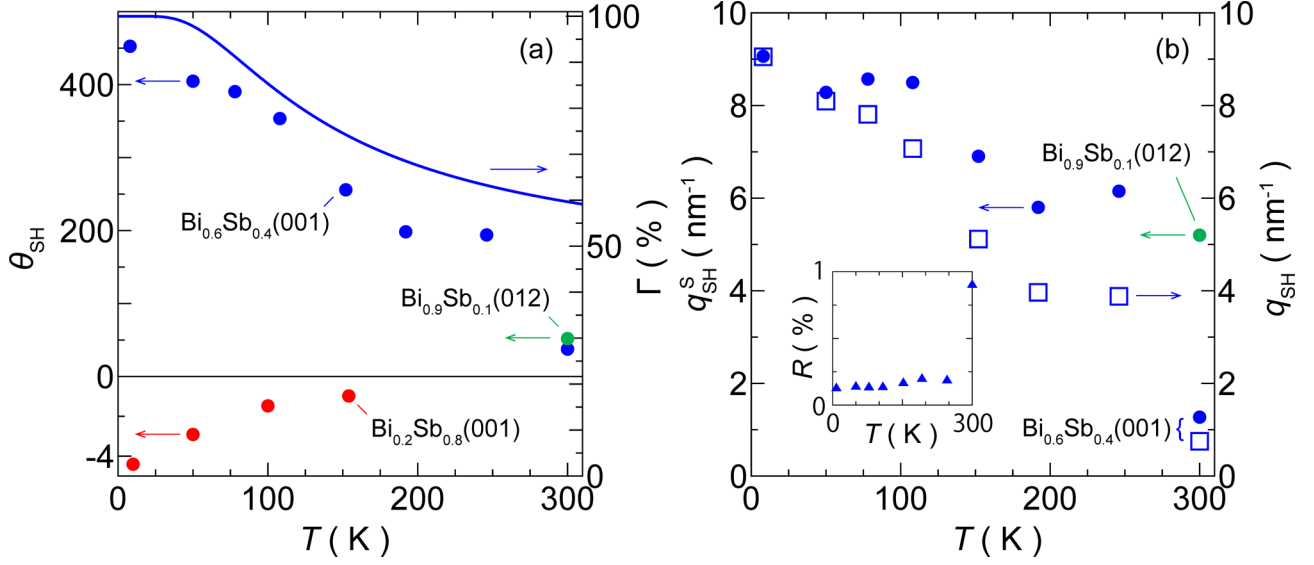


FIG. 4. (a) Temperature dependence of the nominal spin Hall angle θ_{SH} of the 50 nm-thick $\text{Bi}_{0.6}\text{Sb}_{0.4}(001)$ layer in sample A (blue dots) and the 50 nm-thick $\text{Bi}_{0.2}\text{Sb}_{0.8}(001)$ layer in sample B (red dots). Blue line shows the surface contribution factor Γ to the total conductivity in the $\text{Bi}_{0.6}\text{Sb}_{0.4}(001)$ layer. **(b)** Temperature dependence of the nominal sheet spin Hall angle q_{SH} (blue squares) and the surface sheet spin Hall angle q_{SH}^{S} (blue dots) of sample A. Inset shows the temperature dependence of the bulk contribution to the nominal sheet spin Hall angle,

$$R \equiv \frac{2e}{\hbar} \frac{|\sigma_{\text{SH}}^{\text{B}}|}{q_{\text{SH}}(\sigma_{\text{S}}t_{\text{S}} + \sigma_{\text{B}}t_{\text{B}})}. \text{ For a reference, we also show the room-temperature } \theta_{\text{SH}} \text{ and } q_{\text{SH}}^{\text{S}} \text{ of a 10}$$

nm-thick $\text{Bi}_{0.9}\text{Sb}_{0.1}(012)$ layer (green dots in **(a)** and **(b)**).

References

- ¹ Khang, N. H. D, Ueda, Y., Hai & P. N. A conductive topological insulator with large spin Hall effect for ultralow power spin-orbit torque switching. *Nat. Mater.* **17**, 808–813 (2018).
- ² Mellnik, A. R. *et al.* Spin-transfer torque generated by a topological insulator. *Nature* **511**, 449–451 (2014).
- ³ DC, M. *et al.* Room-temperature high spin-orbit torque due to quantum confinement in sputtered $\text{Bi}_x\text{Se}_{1-x}$ films. *Nat. Mater.* **17**, 800-807 (2018).
- ⁴ Fan, Y. *et al.* Magnetization switching through giant spin-orbit torque in a magnetically doped topological insulator heterostructure. *Nat. Mater.* **13**, 699–704 (2014).
- ⁵ Wang, Y. *et al.* Topological surface states originated spin-orbit torques in Bi_2Se_3 . *Phys. Rev. Lett.* **114**, 257202 (2015).
- ⁶ Jamali, M. *et al.* Giant Spin Pumping and Inverse Spin Hall Effect in the Presence of Surface and Bulk Spin-Orbit Coupling of Topological Insulator Bi_2Se_3 . *Nano Lett.* **15**, 7126–7132 (2015).
- ⁷ Kondou, K. *et al.* Fermi-level-dependent charge-to-spin current conversion by Dirac surface states of topological insulators. *Nat. Phys.* **12**, 1027–1031 (2016).
- ⁸ Hsieh, D. *et al.* A topological Dirac insulator in a quantum spin Hall phase. *Nature* **452**, 970–974 (2008).
- ⁹ Nishide, A. *et al.* Direct mapping of the spin-filtered surface bands of a three-dimensional quantum spin Hall insulator. *Phys. Rev. B* **81**, 041309(R) (2010).
- ¹⁰ Roushan, P. *et al.* Topological surface states protected from backscattering by chiral spin texture. *Nature* **460**, 1106–1109 (2009).
- ¹¹ Taskin, A. A. & Ando, Y. Quantum oscillations in a topological insulator $\text{Bi}_{1-x}\text{Sb}_x$. *Phys. Rev. B* **80**, 085303 (2009).
- ¹² Taskin, A. A., Segawa, K. & Ando, Y. Oscillatory angular dependence of the magnetoresistance in a topological insulator $\text{Bi}_{1-x}\text{Sb}_x$. *Phys. Rev. B* **82**, 121302(R) (2010).

- ¹³ Ueda, Y., Khang, N. H. D., Yao, K. & Hai, P. N. Epitaxial growth and characterization of $\text{Bi}_{1-x}\text{Sb}_x$ spin Hall thin films on GaAs(111)A substrates. *Appl. Phys. Lett.* **110**, 062401 (2017).
- ¹⁴ Xiao, S, Wei, D. & Jin, X. Bi(111) thin film with insulating interior but metallic surfaces. *Phys. Rev. Lett.* **109**, 166805 (2012).
- ¹⁵ Kawaguchi, M., *et al.* Current-Induced Effective Fields Detected by Magnetotransport Measurements. *Appl. Phys. Express* **6**, 113002 (2013).
- ¹⁶ Kawaguchi, M. *et al.* Layer thickness dependence of current induced effective fields in ferromagnetic multilayers. *J. Appl. Phys.* **117**, 17C730 (2015).
- ¹⁷ Xu, W. J. *et al.* Scaling law of anomalous Hall effect in Fe/Cu bilayers. *Eur. Phys. J. B* **65**, 233–237 (2008).
- ¹⁸ Liu, L., Moriyama, T., Ralph, D. C. & Buhrman, R. A. Spin-torque ferromagnetic resonance induced by the spin Hall effect. *Phys. Rev. Lett.* **106**, 036601 (2011).
- ¹⁹ Şahin, C. & Flatté, M. E. Tunable Giant Spin Hall Conductivities in a Strong Spin-Orbit Semimetal: $\text{Bi}_{1-x}\text{Sb}_x$. *Phys. Rev. Lett.* **114**, 107201 (2015).
- ²⁰ Teo, J. C. Y., Fu, L. & Kane, C. L. Surface states and topological invariants in three-dimensional topological insulators: application to $\text{Bi}_{1-x}\text{Sb}_x$. *Phys. Rev. B* **78**, 045426 (2008).
- ²¹ Zhu, X. G. *et al.* Three Dirac points on the (110) surface of the topological insulator $\text{Bi}_{1-x}\text{Sb}_x$. *New J. Phys.* **15**, 103011 (2013).

Supplementary Information

Origin of the giant spin Hall effect in BiSb topological insulator

Takanori Shirokura¹, Kenichiro Yao¹, Yugo Ueda¹, and Pham Nam Hai^{1,2,3*}

¹*Department of Electrical and Electronic Engineering, Tokyo Institute of Technology,
2-12-1 Ookayama, Meguro, Tokyo 152-0033, Japan*

²*Center for Spintronics Research Network (CSRN), The University of Tokyo,
7-3-1 Hongo, Bunkyo, Tokyo 113-8656, Japan*

³*CREST, Japan Science and Technology Agency,
4-1-8 Honcho, Kawaguchi, Saitama 332-0012, Japan*

*Corresponding author: pham.n.ab@m.titech.ac.jp

Note 1: Temperature dependence of the resistivity of $\text{Bi}_{0.4}\text{Sb}_{0.6}$ and $\text{Bi}_{0.2}\text{Sb}_{0.8}$

Figure S1 shows the temperature dependence of the resistivity of a $\text{Bi}_{0.4}\text{Sb}_{0.6}$ and a $\text{Bi}_{0.2}\text{Sb}_{0.8}$ single layer (50 nm). The solid line is the fitting curve using Eq. (1) in the main text, which shows that the $\text{Bi}_{0.6}\text{Sb}_{0.4}$ layer behaves as a topological insulator with a band gap of 33.2 meV and mixing of surface and bulk conduction, and that Γ changes from 60 % at 300 K to 100 % at 8 K. Meanwhile, the $\text{Bi}_{0.2}\text{Sb}_{0.8}$ layer behaves purely as a semimetal layer, whose resistivity monotonically decreases with lowering temperature.

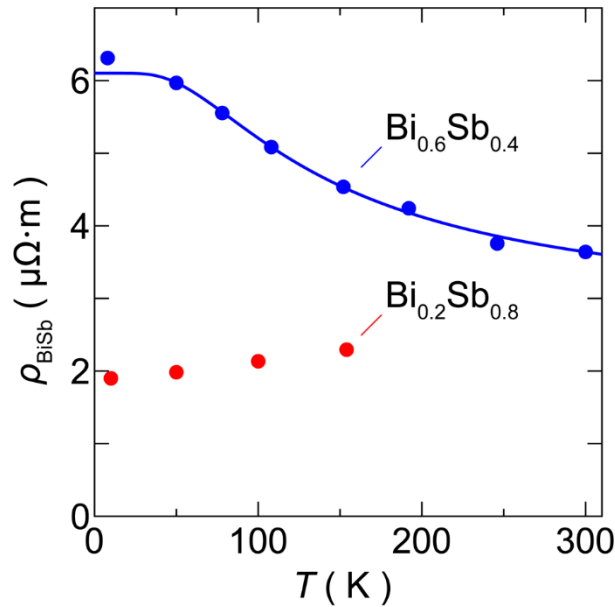


Fig. S1. Temperature dependence of the resistivity of a $\text{Bi}_{0.4}\text{Sb}_{0.6}$ (blue dots) and a $\text{Bi}_{0.2}\text{Sb}_{0.8}$ (red dots) single layer (50 nm). The blue line is the fitting curve using Eq. (1) in the main text.

Note 2: Estimation of the conductivity of the top MnAs layers and the spin Hall angle from the planar Hall resistance

In this work, the MnAs layers are grown on top of the BiSb layers. Thus, its conductivity can be different from that of a single crystalline stand-alone MnAs thin film, and it is not appropriate to use the conductivity of the single crystalline MnAs layer for estimation of the current density in the MnAs and BiSb layers. Here, we estimated the conductivity of the top MnAs layers by comparing the amplitude of their planar Hall resistance to that of a standard 23.3 nm-thick MnAs layer (the

“standard” MnAs) grown on a GaAs(111)B substrate, whose planar Hall resistance as a function of its conductivity was measured in advance at various temperatures. Taking into account the shunt circuit effect of the bias current and short circuit effect of the Hall voltage [1], the planar Hall resistance $R_{\text{PHE}}(\phi)$ of the standard MnAs single layer and that of the MnAs/BiSb bi-layers are given by

$$R_{\text{PHE}}(\phi) = \frac{A(\sigma_{\text{MnAs}})}{t_{\text{MnAs}}} \sin 2\phi, \quad (\text{single layer}) \quad (\text{S1})$$

$$R_{\text{PHE}}(\phi) = \frac{A(\sigma_{\text{MnAs}})}{t_{\text{MnAs}}} \left(\frac{\sigma_{\text{MnAs}} t_{\text{MnAs}}}{\sigma_{\text{MnAs}} t_{\text{MnAs}} + \sigma_{\text{BiSb}} t_{\text{BiSb}}} \right)^2 \sin^2 \psi \sin 2\phi, \quad (\text{bi-layers}) \quad (\text{S2})$$

where $A = \frac{1}{2}(\rho_{\perp} - \rho_{\parallel})$ reflects the magnitude of the planar Hall resistivity and is given by half of the difference between the transverse (ρ_{\perp}) and longitudinal (ρ_{\parallel}) magnetoresistivity [2], σ_{MnAs} and t_{MnAs} are the conductivity and the thickness of MnAs, σ_{BiSb} and t_{BiSb} are the conductivity and the thickness of BiSb, ϕ is the azimuth angle of the magnetization with respect to the charge current direction, and ψ is the polar angle of the magnetization, which is attributed to the z-component of the magnetization arising from the spin-orbit torque. In Eq. (S1) and (S2), A is a function of the conductivity of MnAs, and can be deduced in advance by measuring R_{PHE} and σ_{MnAs} of the single MnAs layer at various temperatures. Thus, we can estimate σ_{MnAs} in the bi-layers by measuring R_{PHE} as shown in Eq. (S2).

By solving the torque balance equation involving the in-plane external field H_{ext} , the spin orbit effective field H_{SO} , and the demagnetising field $H_{\text{deg}} = 4\pi M_{\text{S}}$, we obtain

$$\cos \psi = \frac{H_{\text{so}} \cos \phi}{(H_{\text{ext}} + H_{\text{deg}})}.$$

Thus,

$$\begin{aligned} R_{\text{PHE}}(\phi) &= \frac{A}{t_{\text{MnAs}}} \left(\frac{\sigma_{\text{MnAs}} t_{\text{MnAs}}}{\sigma_{\text{MnAs}} t_{\text{MnAs}} + \sigma_{\text{BiSb}} t_{\text{BiSb}}} \right)^2 \left[1 - \frac{(H_{\text{so}} \cos \phi)^2}{(H_{\text{ext}} + H_{\text{deg}})^2} \right] \sin 2\phi \\ &= \frac{A}{t_{\text{MnAs}}} \left(\frac{\sigma_{\text{MnAs}} t_{\text{MnAs}}}{\sigma_{\text{MnAs}} t_{\text{MnAs}} + \sigma_{\text{BiSb}} t_{\text{BiSb}}} \right)^2 \left\{ \left[1 - \frac{(H_{\text{so}})^2}{2(H_{\text{ext}} + H_{\text{deg}})^2} \right] \sin 2\phi \right. \\ &\quad \left. - \frac{(H_{\text{so}})^2}{4(H_{\text{ext}} + H_{\text{deg}})^2} \sin 4\phi \right\} \end{aligned}$$

The $\sin 4\phi$ term in the bracket is small compared with the $\sin 2\phi$ term and can be dropped. We arrive at

$$R_{\text{PHE}}(\phi) = \frac{A}{t_{\text{MnAs}}} \left(\frac{\sigma_{\text{MnAs}} t_{\text{MnAs}}}{\sigma_{\text{MnAs}} t_{\text{MnAs}} + \sigma_{\text{BiSb}} t_{\text{BiSb}}} \right)^2 \left[1 - \frac{(H_{\text{SO}})^2}{2(H_{\text{ext}} + H_{\text{deg}})^2} \right] \sin 2\phi. \quad (\text{S3})$$

Eq. (S3) shows that the amplitude of $R_{\text{PHE}}^{\text{B}}(\phi)$ (denoted below by $R_{\text{PHE}}^{\text{B}}$) is a quadratic function of H_{SO} :

$$\begin{aligned} R_{\text{PHE}} &= \frac{|A|}{t_{\text{MnAs}}} \left(\frac{\sigma_{\text{MnAs}} t_{\text{MnAs}}}{\sigma_{\text{MnAs}} t_{\text{MnAs}} + \sigma_{\text{BiSb}} t_{\text{BiSb}}} \right)^2 \left[1 - \frac{(H_{\text{SO}})^2}{2(H_{\text{ext}} + H_{\text{deg}})^2} \right] \\ &= R_{\text{PHE-0}} \left[1 - \frac{(H_{\text{SO}})^2}{2(H_{\text{ext}} + H_{\text{deg}})^2} \right] \end{aligned} \quad (\text{S4})$$

$$R_{\text{PHE-0}} \equiv \frac{|A|}{t_{\text{MnAs}}} \left(\frac{\sigma_{\text{MnAs}} t_{\text{MnAs}}}{\sigma_{\text{MnAs}} t_{\text{MnAs}} + \sigma_{\text{BiSb}} t_{\text{BiSb}}} \right)^2 \quad (\text{S5})$$

Eq. (S4) has two very important applications. First, it indicates that R_{PHE} is reduced by

$$\frac{\Delta R_{\text{PHE}}}{R_{\text{PHE}}} = - \frac{(H_{\text{SO}})^2}{2(H_{\text{ext}} + H_{\text{deg}})^2} = - \frac{(\alpha I)^2}{2(H_{\text{ext}} + H_{\text{deg}})^2}, \quad (\text{S6})$$

where α is a proportional constant related to the spin Hall angle, and I is the bias charge current. In heavy metals, H_{SO} is typically small ($\sim 10 \text{ Oe} \cdot \text{MA}^{-1} \text{cm}^{-2}$) compared with H_{deg} , thus the change of R_{PHE} is undetectable. In our case of BiSb, H_{SO} is as large as a few $\text{kOe} \cdot \text{MA}^{-1} \text{cm}^{-2}$ while $H_{\text{ext}} + H_{\text{deg}} = 10 \text{ kOe}$, thus the change of R_{PHE} is detectable. Therefore, H_{SO} can be determined with high certainty by fitting the $\frac{\Delta R_{\text{PHE}}}{R_{\text{PHE}}} - I$ data to Eq. (S6) without the need to know the exact value of

σ_{MnAs} and σ_{BiSb} in the bi-layer (although their exact values can be determined as follows).

To determine σ_{MnAs} , we rewrite Eq. (S5) as

$$R_{\text{PHE-0}} = |A| t_{\text{MnAs}} (\sigma_{\text{MnAs}})^2 \frac{W^2}{(G_{\text{tot}})^2 L^2}, \quad (\text{S7})$$

where G_{tot}, W, L are the total conductance, width, and length of the MnAs/BiSb Hall bars. Let $y = \sigma_{\text{MnAs}}$ a variable to be determined in Eq. (S7), we have

$$|A(y)| * y^2 = \frac{L^2 R_{\text{PHE-0}} (G_{\text{tot}})^2}{W^2 t_{\text{MnAs}}}. \quad (\text{S8})$$

Since the function $A(y)$ is known by measuring in advance the relationship between R_{PHE} and σ_{MnAs} of the standard MnAs single layer in Eq. (S1) at various temperatures, we can deduce y from

the experiment data of $R_{\text{PHE}-0}$.

Fig. S2 shows representative I -dependence of R_{PHE} in sample A and B. The blue dots show the measurement values and the blue solid curves show the fitting to Eq. (S6). Clear quadratic dependence of R_{PHE} on I was observed due to the strong H_{SO} in sample A, as shown in Fig. S2(a) – S2(d). For example, data in Fig. S2(a) yield $\alpha = 0.22$ kOe/mA and $\theta_{\text{SH}} = 530$ at 8 K. However, no clear change of R_{PHE} with I was observed in sample B, in agreement with the smaller SHE in sample B.

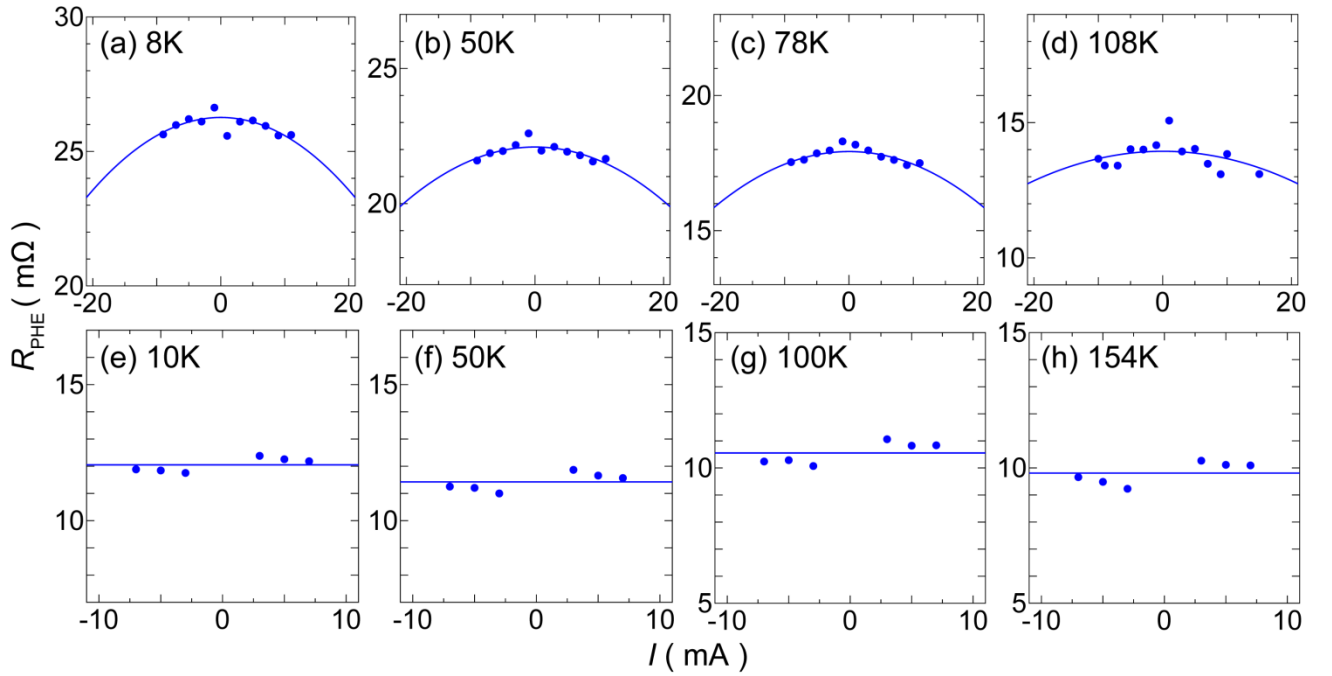


Fig. S2. I -dependence of the planar Hall resistance R_{PHE} for (a) – (d) sample A and (e) – (h) sample B.

Fig. S3(a) shows the relationship between R_{PHE} and σ_{BiSb} of the standard MnAs single layer, which is then used to estimate σ_{MnAs} for sample A and B. The blue dots show the measurement values and the blue solid line shows a fitting curve using a fourth degree polynomial function. σ_{MnAs} is then estimated by solving Eq. (S8) with $R_{\text{PHE}-0}$ obtained from the I -dependence data of R_{PHE} at the $I \rightarrow 0$ mA limit. Fig. S3(b) shows the temperature dependence of σ_{MnAs} in sample A and B, which are then used to estimate J_C and θ_{SH} .

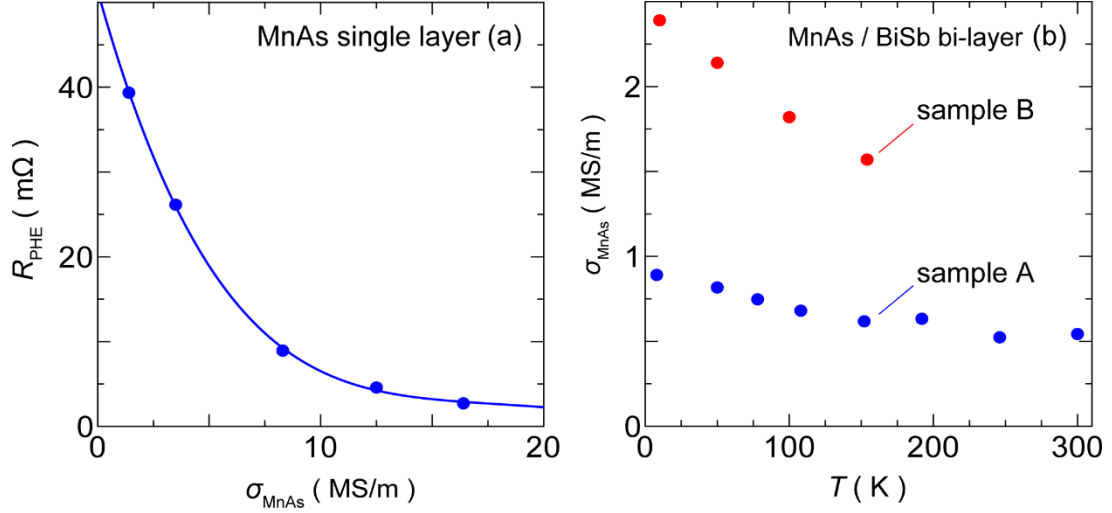


Fig. S3. (a) Relationship between the planar Hall resistance R_{PHE} and the conductivity σ_{MnAs} in a 23.3 nm-thick MnAs single layer. (b) Temperature dependence of the conductivity σ_{MnAs} of the MnAs top layer in the MnAs/BiSb bi-layers.

Note 3: Measurements of $dR_{\text{AHE}}/dH_{\text{perp}}$

In order to estimate H_{SO} from the R_{H}^{SO} data, we need to know the anomalous Hall resistance-magnetic field gradient values at each temperature. This was done by measuring the Hall resistance with a perpendicular magnetic field H_{perp} . In our MnAs/BiSb bi-layer systems, the Hall voltage due to H_{perp} originates from the ordinary Hall voltage from the BiSb layer and the anomalous Hall voltage from the MnAs layer. By considering the shunt circuit effect of the bias current and the short circuit effect of both the Hall voltages [1], the nominal Hall resistance gradient $\frac{dR_{\text{H}}}{dH_{\text{perp}}}$ is given

by

$$\frac{dR_{\text{H}}}{dH_{\text{perp}}} = \frac{dR_{\text{OHE}}}{dH_{\text{perp}}} + \frac{dR_{\text{AHE}}}{dH_{\text{perp}}}$$

$$\frac{dR_{\text{OHE}}}{dH_{\text{perp}}} = \left(\frac{\sigma_{\text{BiSb}} t_{\text{BiSb}}}{\sigma_{\text{MnAs}} t_{\text{MnAs}} + \sigma_{\text{BiSb}} t_{\text{BiSb}}} \right)^2 \left(\frac{dR_{\text{OHE}}}{dH_{\text{perp}}} \right)_0$$

$$\frac{dR_{\text{AHE}}}{dH_{\text{perp}}} = \left(\frac{\sigma_{\text{MnAs}} t_{\text{MnAs}}}{\sigma_{\text{MnAs}} t_{\text{MnAs}} + \sigma_{\text{BiSb}} t_{\text{BiSb}}} \right)^2 \left(\frac{dR_{\text{AHE}}}{dH_{\text{perp}}} \right)_0$$

where $\left(\frac{dR_{\text{OHE}}}{dH_{\text{perp}}} \right)_0$ is the ordinary Hall resistance gradient of the BiSb layer when not in contact with

the MnAs layer, and $\left(\frac{dR_{\text{AHE}}}{dH_{\text{perp}}}\right)_0$ is the anomalous Hall resistance gradient of the MnAs layer when not in contact with the BiSb layer. Thus, $\frac{dR_{\text{AHE}}}{dH_{\text{perp}}}$ can be calculated by subtracting $\frac{dR_{\text{OHE}}}{dH_{\text{perp}}}$ measured in a single BiSb layer from the $\frac{dR_{\text{H}}}{dH_{\text{perp}}}$ value of the bi-layer. Since the anomalous Hall resistance R_{H}^{SO} due to H_{SO} is given by $R_{\text{H}}^{\text{SO}} = \frac{dR_{\text{AHE}}}{dH_{\text{perp}}} H_{\text{SO}}$, we can estimate H_{SO} by $R_{\text{H}}^{\text{SO}} / \frac{dR_{\text{AHE}}}{dH_{\text{perp}}}$.

Table S1 and S2 show the measured values of $\frac{dR_{\text{H}}}{dH_{\text{perp}}}$, $\left(\frac{dR_{\text{OHE}}}{dH_{\text{perp}}}\right)_0$, $\frac{dR_{\text{OHE}}}{dH_{\text{perp}}}$, and $\frac{dR_{\text{AHE}}}{dH_{\text{perp}}}$ of sample A and B at various temperature, respectively. $\frac{dR_{\text{H}}}{dH_{\text{perp}}}$ were measured by sweeping the external magnetic field perpendicular to the substrate. $\left(\frac{dR_{\text{OHE}}}{dH_{\text{perp}}}\right)_0$ were measured in 50 nm-thick single $\text{Bi}_{1-x}\text{Sb}_x$ ($x = 0.4, 0.8$) layers grown on a GaAs(111)A substrate.

Table. S1. Temperature dependence of $\frac{dR_H}{dH_{\text{perp}}}$, $\left(\frac{dR_{\text{OHE}}}{dH_{\text{perp}}}\right)_0$, $\frac{dR_{\text{OHE}}}{dH_{\text{perp}}}$, and $\frac{dR_{\text{AHE}}}{dH_{\text{perp}}}$ of sample A

Sample A				
T (K)	$\frac{dR_H}{dH_{\text{perp}}}$ (m Ω /kOe)	$\left(\frac{dR_{\text{OHE}}}{dH_{\text{perp}}}\right)_0$ (m Ω /kOe)	$\frac{dR_{\text{OHE}}}{dH_{\text{perp}}}$ (m Ω /kOe)	$\frac{dR_{\text{AHE}}}{dH_{\text{perp}}}$ (m Ω /kOe)
8	-21.2	-16.1	-6.60	-14.6
50	-25.6	-23.1	-10.4	-15.1
78	-30.0	-30.6	-15.3	-14.7
108	-34.8	-38.3	-21.2	-13.7
152	-40.0	-45.2	-27.6	-12.4
192	-42.5	-47.2	-29.4	-13.2
246	-39.7	-45.9	-32.0	-7.66
300	-36.7	-40.5	-28.2	-8.52

Table. S2. Temperature dependence of $\frac{dR_H}{dH_{\text{perp}}}$, $\left(\frac{dR_{\text{OHE}}}{dH_{\text{perp}}}\right)_0$, $\frac{dR_{\text{OHE}}}{dH_{\text{perp}}}$, and $\frac{dR_{\text{AHE}}}{dH_{\text{perp}}}$ of sample B

Sample B				
T (K)	$\frac{dR_H}{dH_{\text{perp}}}$ (m Ω /kOe)	$\left(\frac{dR_{\text{OHE}}}{dH_{\text{perp}}}\right)_0$ (m Ω /kOe)	$\frac{dR_{\text{OHE}}}{dH_{\text{perp}}}$ (m Ω /kOe)	$\frac{dR_{\text{AHE}}}{dH_{\text{perp}}}$ (m Ω /kOe)
10	-27.1	29.7	17.8	-44.8
50	-27.8	29.8	18.3	-46.1
100	-28.2	29.2	18.7	-46.9
154	-27.7	27.5	18.1	-45.8

Note 4: Absence of thermoelectric effects

In this note, we present evidences that there is no artifact due to thermoelectric effects that can explain the observed colossal spin Hall angle in sample A. First, we point out that the polarity of θ_{SH} changes from positive (sample A) to negative (sample B). Furthermore, it rapidly decreases from 450 to -4.4, although the top layer in sample A and B is the same MnAs material with slightly different thickness. This cannot be explained by thermoelectric effects whose thermal voltage should have the same magnitude and polarity for both samples.

The strongest evidence of the absence of thermoelectric effects in our MnAs/BiSb bi-layers is the bias current-dependence of the amplitude of the planar Hall resistance R_{PHE} . As shown in Eq. (S6) in Note 2, SHE causes the quadratic dependence of R_{PHE} on I . In contrast, thermoelectric effects, such as the planar Nernst effect, should cause the linear dependence of R_{PHE} on I . However, data in Fig. S2(a)-(d) show clear quadratic and no linear dependence of R_{PHE} on I for sample A. Thus, thermoelectric effects are absent or negligible.

Note 5: Spin Hall angle in the parallel conduction model

The relationship between the spin current and the charge current is given by

$$J_S = \frac{\hbar}{2e} \theta_{\text{SH}} J_C, \quad (\text{S9})$$

where J_S is the spin current density, \hbar is the Dirac's constant, e is the elementary charge, θ_{SH} is the nominal spin Hall angle, J_C is the nominal charge current density. In the case of topological insulators, J_S is generated not only by the current following in the bulk states but also in the surface states. Hence,

$$J_S = \frac{\hbar}{2e} (\theta_{\text{SH}}^{\text{S}} J_C^{\text{S}} + \theta_{\text{SH}}^{\text{B}} J_C^{\text{B}}), \quad (\text{S10})$$

where the symbol S and B represent the surface and bulk contribution, respectively. By considering the parallel conduction model [3] and assuming that the lower surface states not in contact with the MnAs top layer does not contribute to spin current injection, the Eq. (S10) can be

rewritten as

$$J_S = \frac{\hbar}{2e} \left(\frac{\sigma_S t_B}{\sigma_S t_S + \sigma_B t_B} \theta_{SH}^S + \frac{\sigma_B t_B}{\sigma_S t_S + \sigma_B t_B} \theta_{SH}^B \right) J_C, \quad (S11)$$

By comparing Eq. (S9) and Eq. (S11), we obtain

$$\theta_{SH} = \frac{\sigma_S t_B}{\sigma_S t_S + \sigma_B t_B} \theta_{SH}^S + \frac{\sigma_B t_B}{\sigma_S t_S + \sigma_B t_B} \theta_{SH}^B = \Gamma \frac{t_B}{t_S} \theta_{SH}^S + \frac{2e}{\hbar} \frac{\sigma_{SH}^B t_B}{\sigma_S t_S + \sigma_B t_B},$$

where $\Gamma \equiv \sigma_S t_S / (\sigma_S t_S + \sigma_B t_B)$ is the contribution of the surface states to the total conductivity, and

$\sigma_{SH}^B \equiv \hbar \sigma_B \theta_{SH}^B / 2e$ is the bulk spin Hall conductivity.

References

- [1] Xu, W. J. *et al.* Scaling law of anomalous Hall effect in Fe/Cu bilayers. *Eur. Phys. J. B* **65**, 233–237 (2008).
- [2] Mcguire, T. R. & Potter, R. I. Anisotropic Magnetoresistance in Ferromagnetic 3D Alloys. *IEEE Trans. Magn.* **11**, 1018–1038 (1975).
- [3] Xiao, S. *et al.* Bi(111) thin film with insulating interior but metallic surfaces. *Phys. Rev. Lett.* **109**, 166805 (2012).